



OPEN

A novel prediction method for peak cutting force of curved picks considering lithological tolerances

Mingyu Duan^{1,4}, Lefei Shao^{1,4}, Yizhe Huang^{1,2}, Qibai Huang¹, Jiaqi Liu¹ & Zhifu Zhang³✉

This study presents a 3D pick-rock contact calculation method for conical picks, aiming to develop a predictive method with high accuracy and lithological tolerance for peak cutting force (PCF). The method is based on the projection profile method and D. L. Sikarskie stress distribution function. By integrating Griffith's theory with rock damage constitutive model, the energy relationship between the rock fracturing process and crack propagation process is analyzed. Furthermore, in order to accurately correct the PCF, the energy correction function ($C-K_e$) is proposed to calculate the damage intensity index (K_e), which accounts for the relationship between rock brittleness and rock damage elastic-plastic energy. To validate the method, it is compared with full-scale cutting tests and three existing models, and statistical analysis confirms its high lithological tolerance and accuracy, the present model has the highest R^2 of 0.90404, which is at least 12.5% higher relative to the mainstream models. Moreover, incorporating K_e into the method further enhances its predictive capability.

Keywords 3D pick-rock contact calculation method, The rock damage constitutive model, PCF correction method, The damage intensity index, Predictive capability

Abbreviations

PCF	The peak cutting force
UCS	The uniaxial compressive strength
BTS	The Brazilian tensile strength
RMSE	The root mean square error
SE	The standard error
MSD	The mean squared deviation
MAE	The mean absolute error
RSS	The residual sum of squares
α_1	The taper angle of pick body
r_1	The radius of alloy head
r_1	The radius of pick body
h_1	The vertical height of alloy head
h_2	The vertical height of pick body
l_1	The vertical height of point F
l_2	The vertical height of point G
l_3	The vertical height of point C
l_4	The vertical height of point D
γ	The installation angle
d	The cutting depth
a	The long semi-axis
b	The short semi-axis
θ	The horizontal component angle of surface stress
θ_1	The position angle of point M
θ_2	The elliptic tangent angle

¹State Key Laboratory of Digital Manufacturing Equipment and Technology, Huazhong University of Science and Technology, Wuhan 430074, China. ²School of Mechanical Engineering, Hubei University of Technology, Wuhan 430068, China. ³School of Mechanical and Electrical Engineering, Hainan University, Haikou 570228, China. ⁴These authors contributed equally to this work: Mingyu Duan and Lefei Shao. ✉email: 996099@hainanu.edu.cn

ρ_s	The surface energy density
U_0	The energy given by the truncation process
G_s	The energy for new surface
δ	The initial crack size
μ	The rock Poisson's ratio
E	The rock modulus of elasticity
ε_c	The critical strain
K_{Ic}	The rock type I fracture toughness
ϕ	The angle between the surface stress and the cutting profile
K_f	The elastic energy normalization factor
K_e	The damage intensity index
σ_L	The critical fracture stress
C	The brittleness index

Conical picks are widely utilized tools in mining engineering for rock drilling, blasting, excavation, and quarrying operations. Cutters endure high compressive stress, shear stress, and impact loads while also facing corrosion from the coal seam media. Consequently, they become vulnerable components of mining machinery. As rock mining depth and difficulty increase, mining machinery is progressively moving toward automation¹. The theoretical PCF of conical picks offers high precision and high lithological tolerance. It enables efficient selection of cutters, evaluation of work efficiency, and prediction of operational performance. Consequently, it enhances mining efficiency and reduces costs.

The cutting process of cutters corresponds to the evolution of rock damage, including the compaction stage, linear elastic stage, plastic stage, fracture stage, and collapse stage. Various cracks, joints, and defects exist within the rock, leading to the unpredictable and unbalanced nature of the failure process^{2,3}. Rock joints are natural fractures or planar structures formed during geological evolution, and can be classified into parallel and intersecting types. When subjected to external forces or internal stresses, stress within the rock mass concentrates on the joint surfaces. Due to the relatively weak strength of joint surfaces, crack propagation tends to preferentially occur along these surfaces⁴. Additionally, other defects in the rock, such as cracks, pores, and heterogeneities, can induce stress concentration under loading, promoting crack propagation. These defects may also result in water and gas permeation, further accelerating crack propagation. Therefore, in the study of the theoretical prediction of PCF for conical picks, it is essential to consider and analyze how these joints and defects affect rock failure and stability.

According to rock failure mechanisms described above, the cutting force (CF) during the cutting process exhibits dynamic variations. The CF corresponding to the generation of large block fractures in coal and rock is commonly referred to as the PCF, which is influenced by factors such as coal and rock properties, teeth geometry, cutting depth, and cutting angle. Many researchers have investigated the relationship between cutting performance and efficiency of mining machines theoretically, empirically, and numerically.

Evans⁵ conducted a study on the vertical penetration of conical picks into rocks, suggesting that rocks ultimately experience tensile failure. Then he devised a computational model for conical pick cutting forces, showing a strong connection between CF and pick angle, as well as a proportional relationship with the square of the cutting depth and tensile strength of the rock. However, the cutting force was found to be inversely proportional to the rock's brittleness index. Building upon the research findings of Evans, Roxborough and Liu⁶ as well as Goktan⁷ considered the friction between the cutters and the rock and made adjustments to the model. They developed a CF calculation model that included the friction angle between the rock and the cutters. Goktan and Gunes⁸ considered the influence of the cutting angle and proposed a semi-empirical formula for the CF of conical picks based on previous mathematical models. A comparison between calculated and experimental values showed that this model had good predictive performance. Fathipoue-Azar⁹ established a quantitative correlation between rock strength, cutters structural parameters, and average CF by utilizing a data-driven predictive model. This model was based on 157 datasets from 47 rock samples. By considering the nonlinear relationship between the predictor and response variables, an average CF prediction model was developed. Morshedlou et al.¹⁰ established a database of mean cutting forces (MCF) through full-scale testing and subsequently developed a model for predicting cutting forces utilizing regression methods and machine learning models. The results indicate that the model can reasonably predict cutting forces when the input parameters encompass the uniaxial compressive strength (UCS), spacing, Brazilian tensile strength (BTS), penetration depth, cutter tip radius, and tip angle.

Considering the poor stability in solving theoretical models, some researchers conducted extensive studies on the cutting performance of conical picks using experimental and simulation methods. Hekimoglu¹¹ simulated the rock-cutting pattern of alloy heads and delved into the mechanism of teeth breaking. Ranman¹² mathematically described the generation of chips during conical picks rock cutting, dividing the cutting process into three stages: contact, formation of a dense core, and crack propagation leading to rock failure. Copur et al.¹³ discovered a significant statistical relationship between the mechanical indices of rocks obtained from indentation tests and the CF of conical picks. They also observed a satisfactory statistical relationship between CF and the rock's brittleness index.

Bilgin et al.¹⁴ conducted a study based on experimental data obtained from a linear cutting test apparatus. They investigated the relationship between CF, normal force, and rock properties by cutting 22 types of rocks and minerals using conical picks. The research findings indicated that the ratio of CF, normal force, and cutting depth is directly proportional to the compressive strength, tensile strength, and rebound hardness of the rocks. Tiryaki et al.¹⁵ developed a predictive model for average CF using multiple linear regression, multiple nonlinear regression, neural networks, and regression tree methods, based on experimental data from Bilgin et al.¹⁴. Rojek

et al.¹⁶ used the discrete element method to establish uniaxial compressive and Brazilian splitting test models to calibrate the parameters of rocks. Based on this, they created a conical picks rock-breaking model in both two-dimensional and three-dimensional environments. The results showed a good agreement between simulation results and experiments, with better performance in the three-dimensional simulations. Dong et al.¹⁷ utilized PFC^{2D} to examine the characteristics of interparticle force chains in the rock cutting process and delved into the influence of contact state on the cutting force of a single cutter. The conclusion drawn is that the extension of the force chain network aligns with the point contact direction, which is associated with the cutting angle. Su and Akcin¹⁸ developed a discrete element model for cutting rocks with conical picks. The PCF obtained from the simulation presented a strong linear relationship with the measured values. Additionally, there was a good linear relationship between the measured average CF and the calculated values from the theoretical formulas of Evans⁵, Roxborough and Liu⁶, and Goktan⁷. Bao et al.¹⁹ conducted theoretical and experimental studies on the vertical wedging of rocks using conical picks, analyzing it from an energy perspective and employing linear elastic fracture mechanics. They formulated a theoretical model for the Cone Factor, revealing a power-law relationship with an exponent of 4/3 between the CF and cutting depth. Additionally, they observed that approximately 10% of the total work was utilized in the formation of large rock fragments, while the majority of the energy was consumed in the development of a dense core. Furthermore, the research findings suggested that the composition and anisotropy of diverse rock materials influence the propagation of microcracks. Kang et al.²⁰ designed a small-scale rock linear cutting test apparatus that enabled more precise testing of CF. Copur et al.²¹ investigated the impact of various cutting patterns and speeds on the rock-breaking performance of conical picks. Their findings revealed that the double-spiral cutting pattern exhibited the highest efficiency, surpassing both the single-spiral and triple-spiral patterns, while the cutting speed had a minimal influence on the overall cutting performance. Hekimoglu²² proposed calculating the CF and normal force of the cutting tool using the effective area in the cutting diagram. Lu²³ investigated the impact of cutting angle, cutting depth, and other factors on rock fragmentation effectiveness and PCF through LS-DYNA numerical simulations.

In existing cutting force theoretical models, scholars have established PCF calculation models based on specific rock fracture patterns, without systematically considering the influences of the actual shape of conical picks, unstable crack propagation, and rock heterogeneity on calculation performance. However, experimental and simulation results by Coper et al.²¹ indicate that internal rock defects and rock brittleness significantly affect crack propagation and cutting force.

Regarding the energy evolution law of rocks and the effects of external factors on energy evolution, in uniaxial compression conditions, most of the absorbed energy in the rock deformation process is transformed into elastic energy accumulated inside the rock. The energy evolution behavior of rocks exhibits distinct stages, where the accumulation rate of elastic energy increases and then decreases as loading progresses, while the dissipation rate of energy tends to gradually increase²⁴. Zhang²⁵ studied the influence of moisture content and rock properties on the energy evolution of rocks through uniaxial cyclic loading-unloading tests, and they pointed out that the saturation process of rocks reduces the limit of energy absorption and promotes energy dissipation behavior, which was further validated²⁶. The research results on the rock property effect of energy evolution show that the larger the strength and stiffness of the rock, the greater the energy storage limit and the rate of elastic energy growth. The stronger the brittleness characteristic of the rock, the faster and more thorough the release of post-peak elastic energy²⁷. Gao et al.²⁴ studied the energy evolution law of rocks based on uniaxial cyclic loading-unloading tests on rocks with different properties. They further categorized the energy evolution types of rocks into four categories and proposed the rock energy conservation coefficient to quantitatively characterize the energy storage and dissipation characteristics of rocks. The energy evolution characteristics of rocks under different bedding loading angles also exhibit significant differences²⁸. Zhang et al.²⁹ conducted triaxial loading and unloading tests on marble specimens under different stress paths to study the energy evolution characteristics of the rock deformation process, and the results show that the energy storage limit of the rock under triaxial loading is higher than that of uniaxial compression and triaxial unloading, and that bifurcation and chaotic phenomena occur in the energy evolution process in the near-unstable stage.

The current predictive theory of PCF for conical picks is limited by overly simplified calculation models for pick-rock contact, which fail to consider the influences of pick body and crack propagation on CF, as well as the instability of rock damage process, leading to low prediction accuracy and significant dependence on rock properties.

To establish a high lithological tolerance and high prediction accuracy method for PCF, the realistic pick-rock contact situation is considered to establish an accurate 3D model of conical picks by utilizing Box-Lucas curve and piecewise linear functions for alloy head, weld, and pick body profiles, and elliptical analysis for cutting profile determination. The contact surface between pick and rock is layer-integrated, while incorporating the D. L. Sikarskie stress distribution function and Hooke's law, to establish a precise calculation method for the PCF. For the fracture process of rocks with different properties, the energy relationship during crack initiation and propagation is analyzed by using Griffith theory and rock damage constitutive theory, and the fracture stress and damage intensity index (K_c) of PCF are determined. Additionally, considering the relationship between rock brittleness (C) and the energy during the rock damage process, the elastic energy normalization factor (K_f) is introduced to improve the Griffith theory. Finally, to validate the proposed approaches, a comprehensive dataset consisting of 40 full-scale rock-cutting tests is introduced. Among these, 20 samples are designated as the experimental dataset, while the remaining 20 samples are utilized for validation purposes. Based on the experimental dataset, the energy correction function is established between the C and K_f to modify the PCF. The reliability of these modifications is rigorously verified by assessing their performance against the experimental dataset.

A 3D PCF analytical method for curved picks Establishment of a 3D stress analysis model for curved picks

The actual conical pick consists of a curved profile tip, a weld seam, and a tooth body. In this section, the 3D stress analysis model of conical picks is developed based on the projection profile method³⁰.

The contour equation is established by referring to the actual conical picks, and the parameters shown in Fig. 1 are cutting depth d , the vertical distance of the center of the elliptical section h , taper angle of pick body α_1 , radius of alloy head r_1 , the radius of pick body r_2 , installation angle γ and long axis of section ellipse $2a$.

The equations describing the alloy head, weld seam, and generatrix of the pick body profile in the XZ plane are as follows, which are obtained by fitting the Sandvik S-35/80H conical pick with a tip angle of 80 degrees profile using the Box-Lucas model.

$$\begin{cases} z_{OC} = -m + m \cdot e^{nx}, 0 \leq x \leq r_1 \\ z_{CD} = k_1 \cdot x + b_1, r_1 \leq x < r_2 \\ z_{DE} = k_2 \cdot x + b_2, x \geq r_2 \end{cases} \quad (1)$$

where $m = 1.6, n = 0.18, k_1 = 1, b_1 = 9.62, b_2 = -140.89$.

The profile equation for the cutting depth of l can be expressed as:

$$z_{A_1A_2} = -\cot(\gamma) \cdot x + \frac{l}{\cos(\gamma)} \quad (2)$$

By solving the generatrix equation and the profile equation simultaneously, the horizontal coordinate expressions for points A_1 and A_2 at different cutting depths can be obtained. When $l < l_3$, numerical methods are necessary to solve for x_{A_1} and x_{A_2} , while other ranges can be represented using the following equation:

$$x_{A_1} = \begin{cases} \frac{l - b_1 \cdot \cos\gamma}{\cos\gamma \cdot (-k_1 + \cot\gamma)}, l_1 < l < l_2 \\ \frac{l - b_2 \cdot \cos\gamma}{\cos\gamma \cdot (-k_2 + \cot\gamma)}, l > l_2 \end{cases} \quad (3)$$

$$x_{A_2} = \begin{cases} \frac{l - b_1 \cdot \cos\gamma}{\cos\gamma \cdot (k_1 + \cot\gamma)}, l_3 < l < l_4 \\ \frac{l - b_2 \cdot \cos\gamma}{\cos\gamma \cdot (k_2 + \cot\gamma)}, l > l_4 \end{cases} \quad (4)$$

where $l_1 = (-m + m \cdot e^{nr_1} - r_1 \cdot \tan\gamma) \cdot \cos\gamma, l_2 = (k_1 \cdot r_2 + b_1 - r_2 \cdot \tan\gamma) \cdot \cos\gamma, l_3 = (-m + m \cdot e^{nr_1} + r_1 \cdot \tan\gamma) \cdot \cos\gamma, l_4 = (k_1 \cdot r_2 + b_1 + r_2 \cdot \tan\gamma) \cdot \cos\gamma$.

The shape of cross-section A_1-A_2 varies with the cutting depth and is approximately elliptical, as shown in the profile outline in Fig. 2. The long semi-axis a of the approximate ellipse is defined as half the distance between the two intersection points A_1 and A_2 . The short semi-axis b is determined using the following approach: when $l < l_1$ or $l > l_4$, the cross-section forms a standard ellipse, allowing for a direct calculation of the length of b . For the cases of $l_1 < l < l_2, l_2 < l < l_3$, and $l_3 < l < l_4$, by constructing a standard ellipse with B_2 , the midpoint of B_2 and K_2 , and K_2 , the length of b can be obtained (Fig. 2a-c).

The long semi-axes and short semi-axes can be expressed using the following formulas:

$$a = \frac{x_{A_2} - x_{A_1}}{2 \cdot \cos\gamma} \quad (5)$$

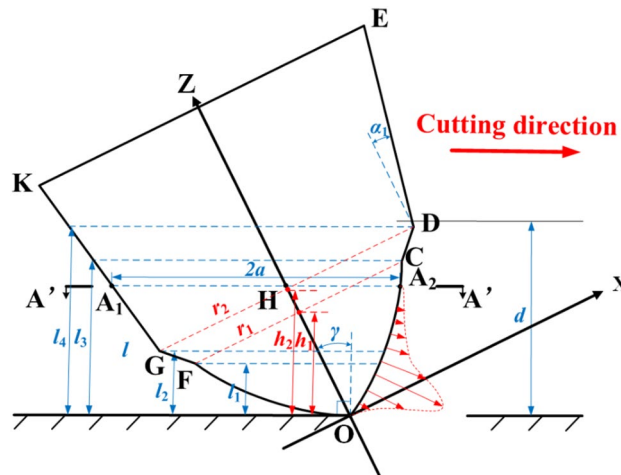


Figure 1. Analysis of contact forces between the conical pick and rock.

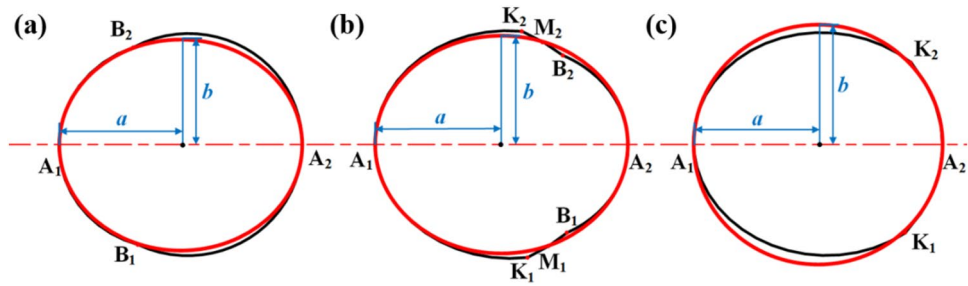


Figure 2. Simplified elliptical profile shape and schematic diagram of long and short axes: (a) for $l_1 < l < l_2$, (b) for $l_2 < l < l_3$, (c) for $l_3 < l < l_4$.

$$b = \begin{cases} \sqrt{\left(\frac{l}{m} \cdot \cos\gamma - \cot\gamma \cdot \frac{x_{A_0}}{m} + 1\right)^2 - x_{A_0}^2}, & 0 < l < l_1 \\ \sqrt{\frac{\frac{r_1^2 - x_B^2}{1 - \frac{x_B^2}{\cos^2\gamma \cdot a^2}}}{\frac{(r_1+r_2)^2 - x_M^2}{1 - \frac{x_M^2}{\cos^2\gamma \cdot a^2}}}}, & l_1 < l < l_2 \\ \sqrt{\frac{\frac{r_2^2 - x_K^2}{1 - \frac{x_K^2}{\cos^2\gamma \cdot a^2}}}{\frac{(r_1+r_2)^2 - x_M^2}{1 - \frac{x_M^2}{\cos^2\gamma \cdot a^2}}}}, & l_2 < l < l_3 \\ \sqrt{\frac{r_2^2 - x_K^2}{1 - \frac{x_K^2}{\cos^2\gamma \cdot a^2}}}, & l_3 < l < l_4 \\ \sqrt{\left(\frac{l}{\cos\gamma} - \cot\gamma \cdot x_{A_0} - b_2\right)^2 - x_{A_0}^2}, & l > l_4 \end{cases}, \quad (6)$$

where, $x_{A_0} = (x_{A_1} + x_{A_2})/2$, $x_B = (l/\cos\gamma + m - m \cdot e^{n \cdot r_1})/\cot\gamma$, $x_K = (l/\cos\gamma + m - m \cdot e^{n \cdot r_2})/\cot\gamma$, $x_M = (x_B + x_K)/2$.

At the installation angle γ and cutting depth l , the cutting profile $A_1J_1A_2J_2$ is shown in Fig. 3.

A coordinate system is established with ellipse midpoint O as the origin for stress distribution analysis (Fig. 4). Within $0 < x < a$ range, each point on the elliptical arc experiences compressive stress from surrounding rocks, perpendicular to the cutting surface. As the pick undergoes a displacement of $d\delta$ along the direction of motion, the normal displacement of each point on the arc $J_1A_2J_2$ decreases from A_2 towards both sides. The normal displacement at any point M on the arc is given by $d\delta \cdot \cos\theta$, where $\cos\theta$ is calculated based on the relationship between the horizontal coordinate of point M and the ellipse tangent.

The relationship between θ_1 and θ_2 can be derived based on the properties of the elliptical tangent, and it is expressed as follows:

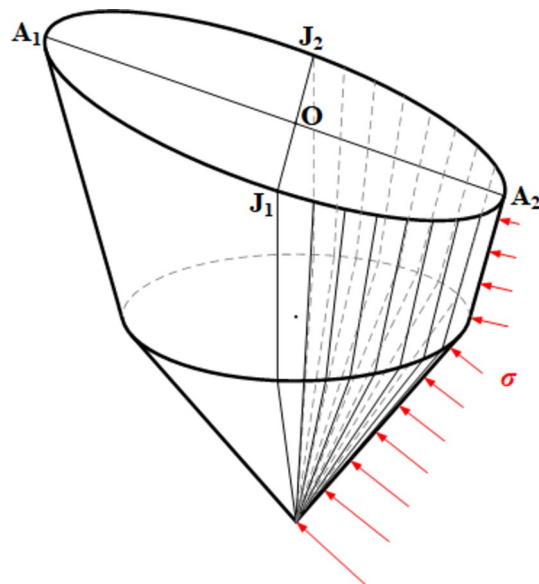


Figure 3. Schematic diagram of cutting profile for conical picks.

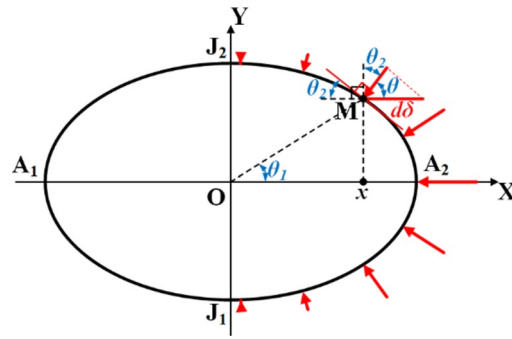


Figure 4. Stress State of the Cutting Profile.

$$\tan\theta_1 \cdot \tan(-\theta_2) = -\frac{b^2}{a^2}. \tag{7}$$

The relationship between $\tan\theta_1$ and the abscissa x can be found as:

$$\tan\theta_1 = \frac{b \cdot \sqrt{1 - (\frac{x}{a})^2}}{x}. \tag{8}$$

The expression for $\tan\theta_2$ can be derived from the equation provided above as follows:

$$\tan\theta_2 = \frac{-bx}{a^2 \sqrt{1 - (\frac{x}{a})^2}}. \tag{9}$$

Based on Fig. 4, it is evident that θ_2 and θ add up to 90° . By combining Eq. (7-9), $\cos\theta$ at the point M on the cutting profile can be given by:

$$\cos\theta = \sin\left(\arctan\left(\frac{-bx}{a^2 \sqrt{1 - (\frac{x}{a})^2}}\right)\right). \tag{10}$$

According to Hooke’s law, the normal stress on the arc $J_1A_2J_2$ decreases from A_2 towards both sides. Therefore, the normal stress at the point M on the cutting profile can be expressed as:

$$\sigma_x = \sigma_{A_2} \cdot \cos\theta. \tag{11}$$

PCF calculation method

During the cutting process of conical picks, intermittent rock fragmentation occurs³¹. The stress distribution along the tip of the conical picks is shown in Fig. 1. Concentrated stress forms at the tip and intensifies as the cutter progresses. Once the concentrated stress exceeds the fracture strength of the rock, cracks initiate at the tip and propagate towards the free surface, resulting in fragmentation. The contact area between the conical picks and the rock exhibits non-uniform distribution across the cutting depth, with a larger contact area nearer to the rock surface. In accordance with D. L. Sikarskie theory³², the stress distribution function on the pick is represented as follows:

$$p_l = \frac{20}{9} \cdot \left(1 - \frac{l}{d}\right)^3 \cdot \left[1 - \cos 2\pi \left(1 - \frac{l}{d}\right)\right], \tag{12}$$

where l is the vertical distance from the stress point A_2 to the tip, d is the cutting depth.

The stress direction on the surface of the conical picks is aligned with the surface normal (Fig. 1). The stress acting at the point A_2 on the pick body is given by:

$$\sigma_{A_2} = \sigma_L \cdot p_l. \tag{13}$$

According to Griffith’s theory, the critical fracture stress σ_L can be determined using the following equation:

$$\sigma_L = \sqrt{\frac{2E\rho_s}{\pi\delta}}, \tag{14}$$

where E is the modulus of elasticity, ρ_s is the surface energy density, which can be determined as:

$$\rho_S = \frac{K_{Ic}^2}{2E} \quad (15)$$

where K_{Ic} is the fracture toughness of rock type I.

By utilizing the peak stresses obtained from Griffith's theory, the stress at point M on the cutting profile, with a cutting depth of l , can be determined (See Fig. 4).

$$\sigma_x = \sigma_L \cdot p_l \cdot \cos\theta = \sqrt{\frac{2E\gamma}{\pi\delta}} \cdot p_l \cdot \cos\theta = \frac{K_{Ic}}{\sqrt{\pi\delta}} \cdot p_l \cdot \cos\theta. \quad (16)$$

According to Eq. (16), it is apparent that the initiation fracture stress of the rock is inversely proportional to the crack size δ . In other words, as the initial crack length increases, the initial cutting stress decreases. During the cutting process, the initial crack undergoes unstable propagation within the rock, leading to fluctuating cutting forces until it reaches a minimum when the rock mass fractures. By integrating the stresses on all cutting profiles within the cutting depth, the CF can be calculated using the following formula:

$$\begin{aligned} PCF &= 2 \int_0^d \int_0^a \sigma_x \cos\varphi \cos\theta \sqrt{1 + \tan^2\theta_2} dx dl \\ &= \frac{2K_{Ic}}{\sqrt{\pi\delta}} \int_0^d \cos\varphi p_l \int_0^a \cos\theta \sqrt{1 + \tan^2\theta_2} dx dl, \end{aligned} \quad (17)$$

where φ represents the angle between the normal stress on the pick surface and the cutting profile.

$$\varphi = \begin{cases} \frac{\pi}{2} - \arctan(abe^{bx_A}) - \gamma, & 0 < l < l_3 \\ \frac{\pi}{2} - \arctan(k_1) - \gamma, & l_3 < l < l_4 \\ \arctan(k_2) - \gamma, & l > l_4 \end{cases}. \quad (18)$$

According to the energy criterion of Griffith's fracture theory, the energy given by the cutting process during crack extension must satisfy the surface energy required to form the new surface of the crack:

$$U_0 \geq G_S, \quad (19)$$

where U_0 is the energy given by the cutting process, and G_S is the surface energy.

Considering the crack as a semicircle with radius δ , the surface energy for the formation of the new surface can be determined as:

$$G_S = \pi\delta^2\rho_S = \frac{\pi\delta^2 K_{Ic}^2}{2E}. \quad (20)$$

Before the rock is cracked, the energy generated by the cutting process is converted into elastic energy and stored in the rock. According to linear elasticity theory, the work done by the cutting process can be written as:

$$U_0 = \int \Delta U dA = 2 \int_0^d \int_0^a \frac{\sigma_x^2}{2E} \cdot \sqrt{1 + \tan^2\theta_2} \cdot K_f dx dl, \quad (21)$$

where K_f is the elastic energy normalization factor.

By substituting the values of U_0 and G_S into Eq. (19), the initial crack size at the moment of crack initiation can be obtained as follows:

$$\delta = \sqrt[3]{\frac{2}{\pi^2} \int_0^d p_l^2 \int_0^a \cos^2\theta \cdot \sqrt{1 + \tan^2\theta_2} \cdot K_f dx dl}. \quad (22)$$

Research findings have unequivocally established that the failure of brittle rocks primarily results in small strains, predominantly in the form of elastic strain^{33,34}. In contrast, plastic deformation in rock leads to strain hardening and substantial plastic deformation. From an energy perspective, the fracturing process in brittle rock is distinguished by a higher allocation of elastic energy, whereas plastic rock exhibits a lower allocation of elastic energy. Notably, the value of K_f , which is intimately linked with rock brittleness, demonstrates an ascending trend as the rock's brittleness escalates.

Substituting δ into Eq. (16) yields the peak cutting force (PCF), which aligns with the cutting direction (as shown in Fig. 1):

$$PCF_0 = \frac{2K_{Ic}}{\sqrt{\pi \sqrt[3]{\frac{2}{\pi^2} \int_0^d p_l^2 \int_0^a \cos^2\theta \cdot \sqrt{1 + \tan^2\theta_2} \cdot K_f dx dl}}} \int_0^d \cos\varphi p_l \int_0^a \cos\theta \sqrt{1 + \tan^2\theta_2} dx dl \quad (23)$$

PCF correction based on rock damage evolution model Constitutive model for rock damage

The inherent intricate composition and structure of rock materials make them inherently susceptible entities³⁵. Therefore, the utilization of damage mechanics and the development of appropriate damage constitutive models

have emerged as effective strategies for investigating rock deformation. In terms of micro-damage mechanics, the representation of the number of internal damage microelements within rocks during the loading process is denoted as N_d . To quantitatively measure this parameter, a statistical damage variable D is introduced, which is defined as the ratio of the number of damaged microelements to the total number of microelements N .

$$D = \frac{N_d}{N}. \quad (24)$$

The failure of a microelement in rock occurs once its stress value reaches the fracture strength. Assuming a normal distribution for the strength of internal microelements in the rock, including the maximum stress values, the failure probability, denoted as $p(\sigma)$, can be defined within a stress interval $[\sigma, \sigma + d\sigma]$.

$$p(\sigma) = \frac{1}{\sqrt{2\pi}m} \exp\left[-\frac{(\sigma - n)^2}{2m^2}\right], \quad (25)$$

where the function $p(\sigma)$ represents the probability density function that describes the strength of the microelement, m denotes the mean value and n represents the standard deviation of the distribution.

When the external load reaches a stress level σ_1 , microelements within the rock that have a strength lower than this level will fail. The cumulative number of failed microelements, denoted as N_d , represents the sum of previously failed microelements in the preceding intervals.

$$N_d = \int_{-\infty}^{\sigma_1} Np(\sigma)d\sigma = NP(\sigma_1), \quad (26)$$

with

$$P(\sigma_1) = \frac{1}{\sqrt{2\pi}\sigma} \int_{-\infty}^{\sigma_1} \exp\left[-\frac{(\sigma_1 - n)^2}{2m^2}\right] dt = \Phi\left(\frac{\sigma_1 - n}{m}\right), \quad (27)$$

where $P(\sigma_1)$ represents the statistical probability function that describes the strength of microelements, and Φ represents the standard normal distribution function.

The statistical damage variable D can be given by:

$$D = P(\sigma). \quad (28)$$

The aforementioned equations, derived from statistical strength theory, illustrates the progression of rock damage. With increasing stress level of σ , the corresponding function value $P(\sigma)$ also increases gradually. Additionally, the statistical probability function $P(\sigma)$ ranges from 0 to 1, reflecting the variation of the damage variable (D).

The stress-strain relationship of brittle rocks follows a two-stage division, governed by the evolution law of rock damage³⁶. Assuming ε_0 represents the strain at the initiation of damage, the constitutive equation for rock damage, derived through the principle of strain equivalence, can be formulated as:

$$\sigma = \begin{cases} E\varepsilon, 0 \leq \varepsilon \leq \varepsilon_0 \\ E(1 - D)\varepsilon, \varepsilon > \varepsilon_0 \end{cases}, \quad (29)$$

where the damage evolution model is given by:

$$D = \begin{cases} 0, 0 \leq \varepsilon \leq \varepsilon_0 \\ \frac{1}{\sqrt{2\pi}\sigma} \int_{-\infty}^{\sigma} \exp\left[-\frac{(\sigma - n)^2}{2m^2}\right] dt = \Phi\left(\frac{\sigma - n}{m}\right), \varepsilon > \varepsilon_0 \end{cases}. \quad (30)$$

Damage intensity index and PCF correction

The Griffith fracture theory is a fundamental explanation of material fracture behavior. It assumes that materials are homogeneous and isotropic, providing insights into crack initiation and suggesting that the critical stress for fracture is related to the initial crack length. However, this theory does not fully account for the direction of crack propagation. In reality, materials often exhibit microstructural variations, anisotropy, and multiple defects, which have a significant impact on fracture behavior. Moreover, the mode of crack propagation is influenced by various factors, including material properties, loading conditions, and stress concentration points³⁷.

Crack propagation is an integral part of the rock failure process, and the evolution of rock damage can be divided into five distinct stages^{4,38}. The rock damage evolution (blue curve) and the stress-strain relationship during the damage process (red curve) are presented in Fig. 5.

- (1) Compaction stage (oa): Under compressive loads, microvoids and cracks within rocks undergo closure as a result of the applied pressure.
- (2) Linear elastic stage (ab): During this stage, rocks display elastic deformation when subjected to external forces. Elastic deformation is reversible, causing the rocks to revert to their original shape and volume once the external force is removed. Rocks exhibit high rigidity and strength in this stage.

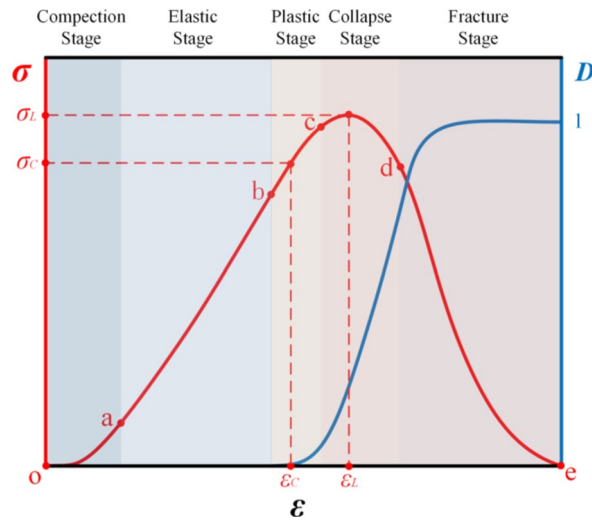


Figure 5. Rock damage evolution process and stress-strain curve.

- (3) Plastic stage (bc): When the external force surpasses the strength limit of the rocks, plastic deformation takes place. In the plastic stage, rocks undergo volume contraction, yielding, and deformation without immediate fracture. The rocks lose the ability for complete elastic recovery in this stage.
- (4) Fracture stage (cd): As the external force continues to increase past the fracture strength of the rocks, cracks and damage begin to manifest. In this stage, cracks inside the rocks gradually expand and connect, forming distinguishable fracture surfaces.
- (5) Collapse stage (de): Once the fractures and cracks in the rock propagate to a certain extent, the overall strength of the rock mass decreases, leading to rock collapse and failure. In the collapse stage, the stability of the rocks is entirely compromised, resulting in the loss of cohesion among rock blocks and substantial destruction and deformation.

The evolution law of rock damage encompasses various stages, starting from the initiation of cracks to their propagation, leading to rock instability and failure. Sustaining continuous crack expansion requires increased energy input due to surface energy requirements. Nevertheless, the unpredictable nature of crack propagation may result in a CF exceeding the crack initiation stage.

To provide a more precise understanding of rock failure behavior, based on the research on the rock damage constitutive model, this paper incorporates the concept of a damage intensity index (K_c). This index allows for the adjustment of the cutting force (CF) at the onset of crack formation in rocks, considering the energy input during the rock failure process and the prevailing conditions during unstable failure.

The area under the stress-strain curve represents the total work performed by external forces on the rock, encompassing both elastic and plastic deformations (See Fig. 5). Considering the influence of rock brittleness on the initial crack size, the elastic energy normalization factor K_f related to rock brittleness is introduced in this paper based on Griffith's theory, which is used to correct the fracture stress. The corrected fracture stress (σ'_f) is incorporated into the damage constitutive equation of the rock in order to compute the damage intensity index K_c .

The damage intensity index K_c is defined as the ratio between the energy needed for crack initiation and the total energy necessary for rock failure, σ is characterized by a damage evolution model that satisfies a normal distribution:

$$K_c = \frac{\int_0^{\epsilon_c} \sigma \, d\epsilon}{\int_0^{\epsilon_e} \sigma \, d\epsilon} = \frac{\int_0^{\epsilon_c} E_0(1-D)\epsilon \, d\epsilon}{\int_0^{\epsilon_e} E_0(1-D)\epsilon \, d\epsilon} \tag{31}$$

In summary, the modified PCF can be represented by the following equation:

$$PCF = K_c \cdot \frac{2K_{Ic}}{\sqrt{\pi} \sqrt[3]{\frac{2}{\pi^2} \int_0^d p_1^2 \int_0^a \cos^2 \theta \cdot \sqrt{1 + \tan^2 \theta_2} \cdot K_f \, dx \, dl}} \int_0^d \sin \varphi \, p_1 \int_0^a \cos \theta \sqrt{1 + \tan^2 \theta_2} \, dx \, dl \tag{32}$$

Based on the Griffith theory and rock damage evolution theory, there is a strong correlation between the rock brittleness index (C) and the elastic energy normalization factor (K_f). Taking the elastic modulus (E) and uniaxial compressive strength (UCS) of rocks as references, the relationship between C and K_f is fitted to 20 sets of experimental data of full-size rock cuts selected on the basis of the research results of Belgin. This relationship is then extended and applied to the correction of PCF.

A comprehensive overview of the crucial parameters pertaining to the rock samples, test conditions, and corresponding results observed across the selected 20 test cases is presented in Table 1. The tests are conducted

No	Rock Type	E(GPa)	UCS(MPa)	BTS(MPa)	K _{Ic}	ε _c	γ	d	PCF ₀	PCF	PCF _{exp}	K _c	K _f	C
1	Chromite-1	3.5	32	3.7	0.64	0.0135	35	5	3.13	8.14	7.16	2.60	0.4497	0.8231
2	Copper-1	4.2	33	3.4	0.62	0.0130	35	5	3.48	7.87	4.40	2.26	0.1958	0.8458
3	Copper-2	4.96	41	5.7	0.85	0.0129	35	5	3.64	12.37	7.33	3.39	0.9874	0.8043
4	Anhydrite	11	82	5.5	1.13	0.0103	35	5	9.73	14.24	12.52	1.46	0.0150	0.9255
5	Sandstone-1	17	114	6.6	1.41	0.0076	35	5	13.46	18.14	19.69	1.35	0.0081	0.9517
6	Sandstone-2	28	174	11.6	2.15	0.0095	35	5	20.55	31.60	23.25	1.54	0.0080	0.9677
7	Tuff2	1.4	11	1.2	0.25	0.0138	35	5	1.07	3.11	7.08	2.91	0.9987	0.8154
8	L chromite	2.9	46	3.7	0.74	0.0175	35	5	4.53	8.90	8.71	1.96	0.1167	0.8699
9	Harsburgite	2.1	58	5.5	0.97	0.0314	35	5	4.54	14.88	14.97	3.28	0.5864	0.8427
10	Limestone	57	121	7.8	1.55	0.0029	35	5	14.25	21.22	21.51	1.49	0.0101	0.9926
11	Chromite-1	3.5	32	3.7	0.64	0.0135	35	9	6.43	14.30	14.83	2.22	0.4512	0.8231
12	Copper-1	4.2	33	3.4	0.62	0.0130	35	9	7.16	13.44	15.07	1.88	0.1963	0.8458
13	Copper-2	4.96	41	5.7	0.85	0.0129	35	9	7.49	21.92	25.82	2.92	0.9919	0.8043
14	Anhydrite	11	82	5.5	1.13	0.0103	35	9	20.04	20.04	16.30	1.00	0.0150	0.9255
15	Sandstone-1	17	114	6.6	1.41	0.0076	35	9	27.71	29.81	29.52	1.08	0.0081	0.9517
16	Sandstone-2	28	174	11.6	2.15	0.0095	35	9	42.29	47.17	48.10	1.12	0.0080	0.9677
17	Tuff2	1.4	11	1.2	0.25	0.0138	35	9	2.20	5.40	11.84	2.45	0.9985	0.8154
18	L chromite	2.9	46	3.7	0.74	0.0175	35	9	9.32	16.10	16.24	1.73	0.1166	0.8699
19	Harsburgite	2.1	58	5.5	0.97	0.0314	35	9	9.33	27.01	26.91	2.89	0.5873	0.8427
20	Limestone	57	121	7.8	1.55	0.0029	35	9	29.33	33.07	32.85	1.13	0.0101	0.9926

Table 1. Rock characteristic parameters in cutting tests and calculation results of PCF.

using Sandvik S-35/80H conical pick with a tip angle of 80 degrees and an alloy head diameter of 20 mm. The cutting angle is set at 55 degrees, and the cutting speed is 12.7 cm/s¹⁴. In Table 1, *E* is the modulus of elasticity, *UCS* is the uniaxial compressive strength, *BTS* is the uniaxial tensile strength, *K_{Ic}* is the type I fracture toughness, *ε_c* is the critical strain, *γ* is the mounting angle, *d* is the cutting depth, *PCF₀* is the pre-correction peak cutting force, *PCF* is the corrected peak cutting force, *PCF_{exp}* is the experimental value, *K_c* is the damage intensity index, *K_f* is the elastic energy normalization factor, *C* is the rock brittleness index.

A nonlinear equation system is constructed based on the *UCS*, *ε_c*, and the damage evolution model (See Eq. 30) of the rock samples' parameters from the 20 cutting tests. By solving for the distribution coefficients (*m* and *n*) of the normal distribution, both the stress–strain curve during the rock damage process and the evolution curve of the damage variable (Fig. 5) are established. Through the integration of Eqs. (31, 32), and the obtained damage evolution model, the corrected PCF can be determined.

For the Griffith theory and rock damage evolution theory, *K_f* is only related to the rock type and independent of the cutting depth. Based on the strong correlation between *K_f* and *C*, there exists an optimal *K_f* and *K_c* that accurately reflect the rock's failure characteristics under different rock brittleness conditions, leading to the precise correction of PCF. By solving Eqs. (14, 15, 22), an expression for fracture stress incorporating *K_f* can be derived.

$$\sigma_{L'} = \frac{2K_{Ic}}{\sqrt{\pi \sqrt[3]{\frac{2}{\pi^2} \int_0^d p_l^2 \int_0^a \cos^2 \theta \cdot \sqrt{1 + \tan^2 \theta_2} \cdot K_f dx dl}}} \tag{33}$$

The fracture stress (*σ_{L'}*) corrected in relation to *K_f* should not surpass the *UCS* of the rock. To ensure this, the *K_c* is determined within a suitable range of *K_f* for each rock sample, resulting in the correction of PCF. The theoretical PCF values derived from the 20 experimental sets showed the highest accuracy compared to the experimental PCF values. The corresponding data are meticulously recorded in Table 1, facilitating a comprehensive evaluation of the fitting accuracy.

The brittleness index considered in this study incorporates the elastic modulus, uniaxial compressive strength, and tensile strength as contributing factors in Eq. (34). A lower value of the brittleness index indicates a higher degree of brittleness in the rock. The relationship between *C* and *K_f* can be determined using Allometric function fitting (See Fig. 6).

$$C = \frac{e^{\frac{E}{20000} \cdot \sigma_c - \sigma_t}}{e^{\frac{E}{20000} \cdot \sigma_c + \sigma_t}} \tag{34}$$

where *σ_t* represents the tensile strength of the rock, *σ_c* refers to the uniaxial compressive strength of the rock.

The elastic energy normalization factor can be expressed in terms of the brittleness index *C* as follows:

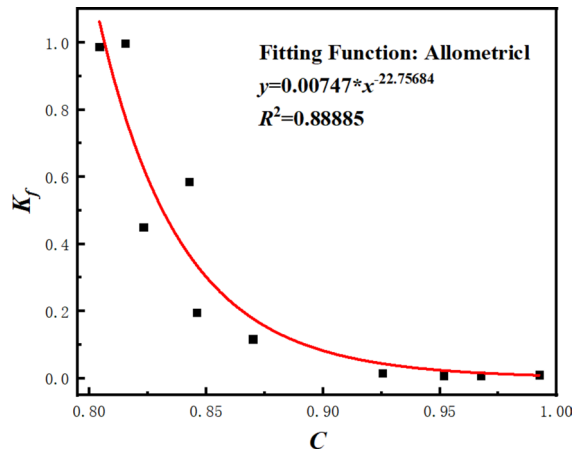


Figure 6. Energy correction function fitted by C and K_f .

$$K_f = a \cdot C^b = 0.00747 \cdot \left(\frac{e^{\frac{E}{20000} \cdot \sigma_c - \sigma_t}}{e^{\frac{E}{20000} \cdot \sigma_c + \sigma_t}} \right)^{-22.75684} \quad (35)$$

Through the correlation analysis, the determination coefficient is 0.89, indicating a strong predictive capability of the independent variable C in the regression model for the dependent variable K_f . Furthermore, a two-tailed t -test is performed on the two parameters with a confidence level of 0.05, as presented in Table 2. The degree of freedom of the sample is 8 and the level of significance is 0.05. The critical value t_L is determined to be 2.306 based on the t -test critical value table. Significantly, both the absolute values of the t -statistics for the two parameters exceed t_L , while the corresponding probability (p -value) for the larger absolute t -value is considerably smaller than 0.025. These findings suggest that both parameters are crucial in the model, playing significant roles in interpreting and fitting the data. In Table 2, SE is the standard error.

The energy correction function, obtained from the relationship between C and K_f along with the determination coefficient and t -test results, clearly demonstrate the strong correlation exhibited by the C and the K_f . For rocks with known lithological parameters, the brittleness index can be solved to characterize the rock's brittleness, and the elastic energy normalization factor K_f can be calculated through this function. In further analysis, in conjunction with the rock's constitutive equation, the damage intensity index K_e can be used to modify the theoretical PCF. The solutions for C , K_f , and K_e for each rock sample are listed in Table 1.

To verify the reliability of the damage intensity index K_e , the discrete element method is used to perform microparameter matching with each lithological parameter under the same cutting conditions. Subsequently, discrete element simulations (PFC^{2D}) are performed using conical picks with linear cutting (Fig. 7). During each cutting cycle, the cutting force acting on the pick at the point of first crack initiation is considered as the fracture CF. Furthermore, the highest CF observed within one cycle of rock failure is regarded as the PCF. Over 5 cutting

Parameters	Value	SE	t -value	p -value > t	t_L
A	0.00747	0.00138	5.41	0.00063836	2.306
b	-22.75684	5.20751	-4.37	0.0023805	

Table 2. t -value test of energy correction function.

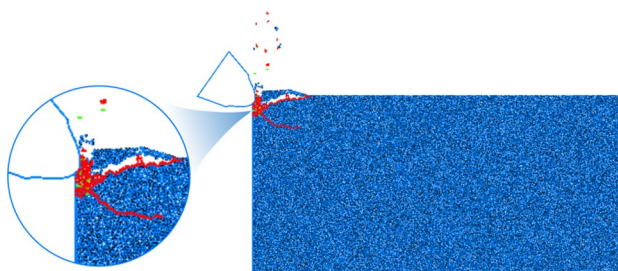


Figure 7. Simulation of conical pick linear cutting test using PFC.

cycles, the fracture CF, PCF, and their averages are recorded. Finally, the value of K_c is determined based on the simulations results.

For each cutting stage of the simulation process, as the conical pick compresses the rock, the CF increases linearly while the number of cracks remains constant, corresponding to the elastic stage. By detecting the change in the number of cracks, the CF corresponding to the initial stage of continuous crack growth is identified as the fracture CF, which coincides with the computed fracture stress in this work. The PCF during the process of crack propagation and rock block detachment inside the rock is recorded as illustrated in Fig. 8. The ratio of the average PCF to the average fracture CF over 5 cycles is then calculated as the corresponding K_c for the rock sample, consistent with the calculation process of the theoretical method. Based on the PFC simulation results for 20 different cutting conditions, it can be observed that for cutting depths of 5 and 9 mm, the simulated results of the damage intensity index exhibit the same trend as the theoretical solutions, with a maximum error of less than 15%, as depicted in Fig. 9. This finding demonstrates the agreement between simulation and theoretical calculations, providing initial validation for the reliability of employing the energy correction function ($C - K_f$) to modify the PCF method.

In order to investigate the effect of C , K_f and K_c on the prediction accuracy of PCF, the sensitivity of PCF to the three parameters is calculated numerically by combining Eqs. (31,32,34,35). C , K_f and K_c are varied up and down by 10%, and the corresponding PCF values are calculated, and the sensitivity results are recorded in Table 3 and Fig. 10.

Drawing upon the aforementioned findings, a significant influence of increased rock brittleness (C) on the PCF is observed, leading to a considerable surge in its values. Furthermore, the impact of K_c on PCF calculations appears to be comparatively minor. Additionally, Eq. (32) and Fig. 10 suggest that K_c serves as a proportional correction factor for PCF. In summary, rock brittleness (C) has the utmost significance on PCF prediction outcomes, followed by K_c , whereas K_f exerts the least influence on PCF prediction results.

The correlation between the theoretical uncorrected and corrected PCF values and the experimental PCF values is illustrated in Fig. 11. To evaluate the predictive capabilities of the method proposed in this study against existing models, this paper introduces the Evans model Eq. (36), Roxborough model Eq. (37), and Goktan

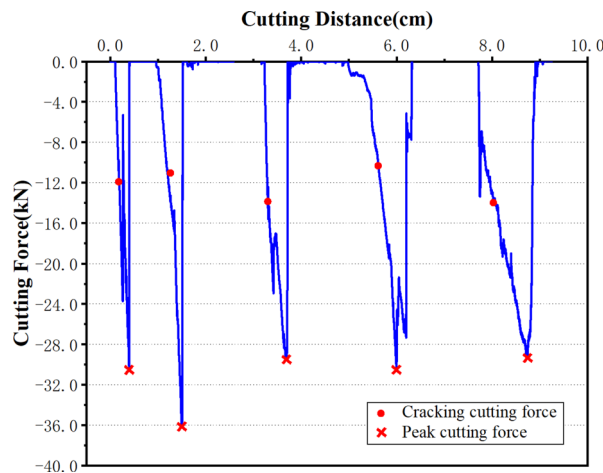


Figure 8. Variation of cutting force with cutting distance.

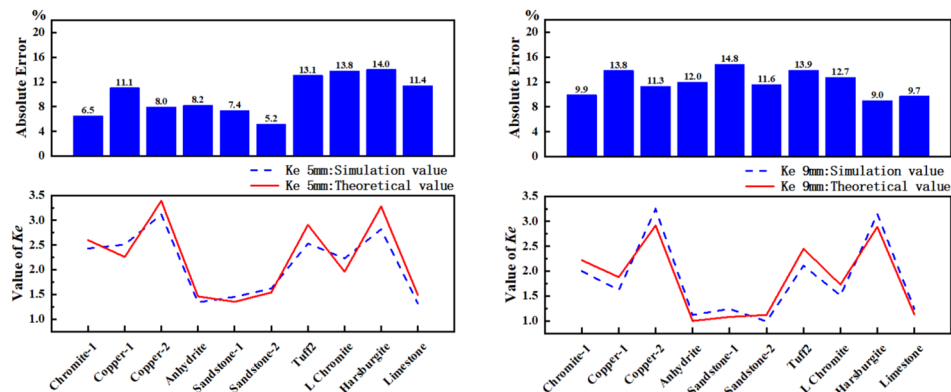


Figure 9. Comparison between theoretical and simulated calculation of K_c .

Type	C	K_f	K_e	PCF	$\Delta PCF/PCF$	Sensitivity
Original	0.8231	0.4497	2.6	8.14	0	0
+ ΔC	0.9054	0.4497	2.6	7.72	-0.052	-0.52
- ΔC	0.7408	0.4497	2.6	9.37	0.214	-2.14
+ ΔK_f	0.8231	0.4947	2.6	9.77	0.042	0.42
- ΔK_f	0.8231	0.4047	2.6	8.86	-0.093	0.93
+ ΔK_e	0.8231	0.4497	2.86	9.75	0.100	1.00
- ΔK_e	0.8231	0.4497	2.34	8.77	-0.100	1.00

Table 3. Sensitivity analysis of PCF to C, K_f and K_e .

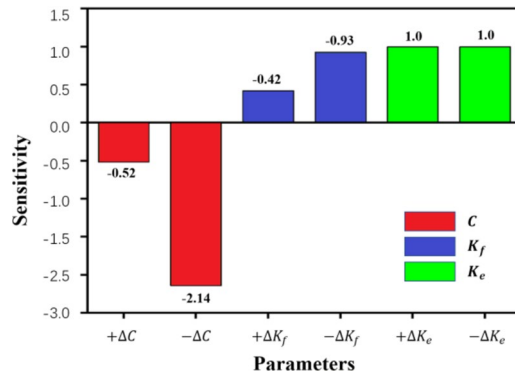


Figure 10. Comparison between theoretical and simulated calculation of C, K_f and K_e .

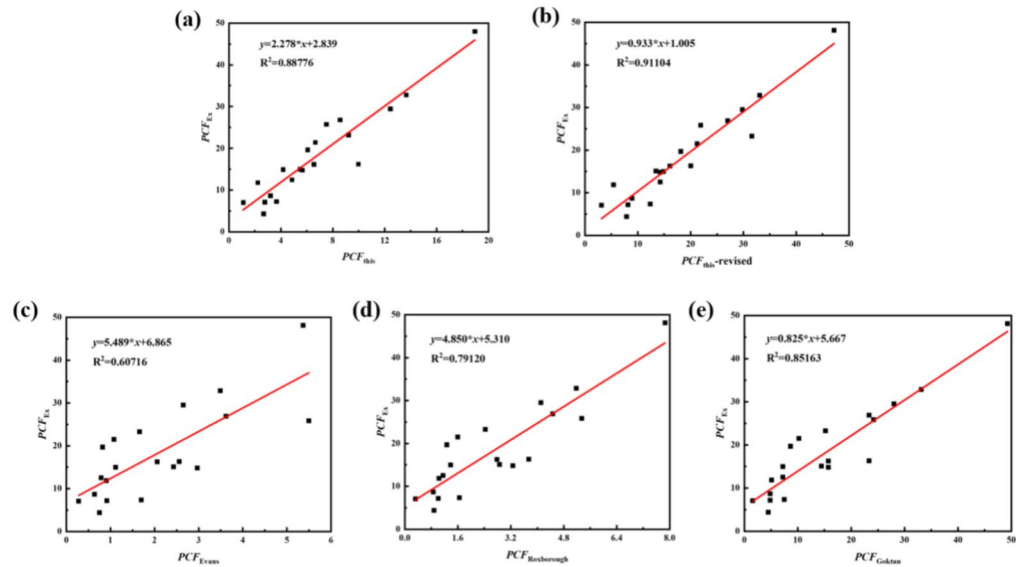


Figure 11. Results of correlative analysis between theoretical model calculation results and experimental results. (a) the uncorrected method of this paper, (b) the corrected method of this paper, (c) Evans model, (d) Roxborough model, (e) Goktan Semi-empirical model.

semi-empirical model Eq. (38) and the corresponding PCF values for the samples based on these models are calculated. The correlations between the predicted values of each model and the experimental values are presented in Table 4.

$$PCF = \frac{16\pi\sigma_t^2 \cdot d^2}{\cos^2\alpha \cdot \sigma_c}, \tag{36}$$

PCF model	This method (uncorrected)	This method (corrected)	Evans	Roxborough	Goktan
R^2	0.88776	0.91104	0.60716	0.7912	0.85163
$RMSE$	3.67451	3.27134	6.87439	5.01181	4.112
RSS	243.03676	192.63038	850.6294	452.12875	304.3541

Table 4. Comparison of prediction accuracy among different models. Significant values are in bold.

where σ_t represents the tensile strength of the rock, d denotes the cutting depth, and σ_c refers to the uniaxial compressive strength of the rock.

$$PCF = \frac{16\pi\sigma_c d^2 \sigma_t^2}{(2\sigma_t + (\sigma_c \cos\alpha / [(1 + \tan f) / \tan\alpha]))^2}, \tag{37}$$

where f denotes the friction angle between the pick and the rock.

$$PCF = \frac{4\pi\sigma_t d^2 \sin^2(\alpha + f)}{\cos(\alpha + f)}. \tag{38}$$

Based on the data presented in Table 4, the uncorrected method proposed in this paper shows superior performance in terms of R^2 , $RMSE$, and RSS when compared to other models. Furthermore, the corrected method demonstrates a significant improvement over the uncorrected method. The specific analysis is as follows:

- (1). Coefficient of determination (R^2): The uncorrected method in this study has a coefficient of determination of 0.88776, which increased to 0.91104 after correction. The corrected method demonstrates superior performance compared to the uncorrected one, exhibiting a 2.6% increase in the coefficient of determination. This implies that the corrected method is capable of explaining a higher proportion of the variance in the dependent variable.
- (2). Root mean square error ($RMSE$): The initial method had an $RMSE$ of 3.67451, which decreased to 3.27134 after correction. The corrected method has a smaller $RMSE$ compared to the uncorrected method, indicating higher predictive accuracy and reduced differences between the predicted and actual values.
- (3). Residual sum of squares (RSS): The initial method had an RSS of 243.03676, which decreased to 192.63038 after correction. This reduction of 20.7% in the RSS implies an improved model fit and decreased prediction errors in the corrected method.

The corrected method exhibits an increase in R^2 and a decrease in both $RMSE$ and RSS , indicating enhanced accuracy and effectiveness in predicting and explaining the data. Overall, the corrected method demonstrates superior performance compared to other models.

To further validate the validity of the linear relationship between the theoretical calculation results obtained from the regression analysis and the experimental values, a variance analysis was conducted at a 95% confidence level. In the analysis, the experimental results and theoretical calculation values are treated as the dependent and independent variables, respectively. The analysis results, presented in Table 5, demonstrate that the P -value in the F -test for the linear relationship between the calculation results of the five models and the experimental results

Model	DF	Sum of squares	MSD	F -value	P -value	
This method (uncorrected)	Model	1	1922.28814	1922.28814	142.37017	5.53044×10^{-10}
	Error	18	243.03676	13.50204		
	Sum	19	2165.3249			
This method (corrected)	Model	1	1972.69452	1972.69452	184.3349	6.74877×10^{-11}
	Error	18	192.63038	10.70169		
	Sum	19	2165.3249			
Evans	Model	1	1314.6955	1314.6955	27.82001	5.14552×10^{-5}
	Error	18	850.6294	47.25719		
	Sum	19	2165.3249			
Roxborough	Model	1	1713.19615	1713.19615	68.2052	1.55315×10^{-7}
	Error	18	452.12875	25.11826		
	Sum	19	2165.3249			
Goktan	Model	1	1860.9708	1860.9708	110.06086	4.24994×10^{-9}
	Error	18	304.3541	16.90856		
	Sum	19	2165.3249			

Table 5. Analysis of variance for models.

is significantly less than 0.05. This indicates that the linear correlations obtained from the regression analysis are all valid. In Table 5, *MSD* is the mean squared deviation.

According to the aforementioned results, the corrected method demonstrates superior predictive performance compared to other models, as it exhibits closer alignment with actual data. Moreover, the corrected method shows significant improvement over the uncorrected one.

The improvement is mainly caused by the following factors:

- (1). Refinement of fracture conditions: Existing theories assume specific bedding structures or follow specific rock fragmentation patterns, and only consider one or two rock parameters to differentiate rock properties. This limited approach results in a lack of universality in predictive theories of PCF. In contrast, the Griffith theory used in this study determines the crack initiation length for rocks of different types from an energy perspective. It incorporates multiple rock parameters such as elastic modulus, K_{Ic} , and *UCS* to consider the influence of rock properties on elastic energy and surface energy. As a result, it exhibits enhanced adaptability to rocks with diverse bedding structures and fragmentation forms.
- (2). Accurate modeling of conical picks: The conical pick consists of a pick tip, a weld, and a pick body, with the pick tip having a curved profile and the pick body having a straight profile. Existing theories simplify the conical pick as a two-dimensional pick tip model within a plane, primarily considering the cutting stresses between the tip and the rock. In contrast, the model in this study is based on the projection contour method combined with a simplified elliptical profile. It comprehensively analyzes the stress distribution in both the axial and radial directions of the pick, thereby accurately reproducing the cutting stresses on the conical surface of the pick to the greatest extent.
- (3). Realistic stress distribution function: Based on the research results of D. L. Sikarskie stress-optical experiments on the pick surface, the D. L. Sikarskie stress distribution function is the closest match to the experimental results. The method in this study relies on this theory when analyzing the axial forces on the pick teeth, while the theories proposed by Evans, et al., assume a linear decrease in teeth tip forces, which is an idealized hypothesis lacking experimental evidence.
- (4). Energy-based crack propagation law: The rock fragmentation process varies significantly for different rock types and bedding structures, and the crack propagation process is highly unstable. Existing theories founded on specific fragmentation laws, resulting in the instability of predictive outcomes. In contrast, the method in this study evaluates the energy relationship between rock crack initiation and propagation stages based on the Griffith theory and the destruction intensity index, grounded in physical principles. Therefore, it can accurately describe the rock crack initiation and propagation processes.

Based on the above analysis, rocks with varying lithologies and bedding structures demonstrate substantial distinctions in the fracturing process, characterized by highly unstable crack propagation. Existing theories proposed by Evans et al., with their reliance on specific fragmentation patterns, exhibit significant inaccuracies. In contrast, the energy relationship governing the onset of rock fracture and subsequent crack propagation stages can be more accurately described by utilizing the Griffith theory and damage intensity index.

Reliability verification of energy correction function

Based on the research in Sect. “[Damage intensity index and PCF correction](#)”, the elastic energy normalization factor can be mathematically expressed by utilizing the brittleness index (See Eq. 35).

This section presents the verification of the reliability of the correction process based on 20 data sets. Table 6 lists the rock sample parameters, test conditions, and experimental results used, where rock numbers 1–12 are quoted from the Belgian study and rock numbers 13–20 are obtained by rock mechanical properties test and single-tooth cutting tests, see Figs. 12, 13.

Figure 12 shows the material performance test of gritstone, which is carried out on the TENSION concrete pressure test machine. Figure 12b shows the uniaxial compression test of red gritstone with loading speed of 0.2 mm/min and specimen size of $\Phi 50 \times 100$ mm. Figure 12c conducts the Brazilian splitting test under axial loading of disc-shaped specimen with specimen size of $\Phi 50 \times 25$ mm. The single-tooth cutting test is shown in Fig. 13. Single-tooth cutting experimental bench with hydraulic drive unit, drive the rock body to do straight-line movement, while the tool is fixed mounted on the gantry, to achieve a fixed depth of linear cutting. The tests are conducted using AID-U95-25 conical pick with a tip angle of 90 degrees and an alloy head diameter of 15.5 mm. The cutting angle is set at 40 degrees, and the cutting speed is 12.7 cm/s.

For each rock sample, the damage evolution model, which follows a normal distribution, is derived using *UCS* and critical strain (ϵ_c). The elastic energy normalization factor (K_f) is calculated using Eq. (35), while the damage intensity index (K_c) is determined by Eq. (31). The results of the calculations are summarized in Table 6.

To assess the accuracy and performance of the regression model, correlation analysis is conducted on five models. The mean absolute error (*MAE*) and root mean square error (*RMSE*) are computed to measure the disparity between the calculated values and experimental values. Results are presented in Table 7. Among the validation set, the current method demonstrates superior predictive ability compared to other models. The uncorrected method in this study achieves a coefficient of determination (R^2) of 0.81591. After applying the correction function derived in Sect. “[Damage intensity index and PCF correction](#)”, the R^2 increases to 0.90404, indicating a 10.8% improvement over the initial value. Besides, the mean absolute error (*MAE*) decreases by 34.8%, and the root mean square error (*RMSE*) decreases by 20.8%, indicating a better model fit to the experimental data.

In conclusion, based on statistical analysis and evaluation metrics, it is evident that the current method surpasses other models in terms of its predictive capability for the validation set. Moreover, the corrected method exhibits enhanced performance, characterized by smaller prediction errors and better fitting, consequently

No	Rock	E (GPa)	UCS(MPa)	BTS(MPa)	K_{Ic}	ϵ_c	γ	d	C	K_f	K_c	PCF ₀	PCF	PCF _{exp}
1	Trona	3.4	30	2.2	0.49	0.0134	35	5	0.8835	0.0725	2.02	3.25	6.57	3.88
2	Sandstone-3	33.3	87	8.3	1.38	0.0036	35	5	0.9645	0.0348	1.46	10.33	15.13	9.09
3	Tuff1	1.1	10	0.9	0.21	0.0139	35	5	0.8430	0.3679	2.14	1.06	2.27	2.05
4	Tuff3	2.4	27	2.6	0.51	0.0139	35	5	0.8426	0.1021	1.42	3.19	4.54	3.77
5	Tuff4	1.6	14	1.5	0.30	0.0138	35	5	0.8200	0.8094	2.91	1.33	3.87	2.83
6	Tuff6	0.4	6	0.2	0.09	0.0187	35	5	0.9367	0.0573	2.03	0.62	1.26	1.33
7	Trona	3.4	30	2.2	0.49	0.0134	35	9	0.8835	0.0727	1.68	6.68	11.19	12.26
8	Sandstone-3	33.3	87	8.3	1.38	0.0036	35	9	0.9645	0.0348	1.00	21.26	21.26	15.92
9	Tuff1	1.1	10	0.9	0.21	0.0139	35	9	0.8430	0.3683	1.79	2.18	3.90	4.02
10	Tuff3	2.4	27	2.6	0.51	0.0139	35	9	0.8426	0.1022	1.09	6.57	7.13	7.22
11	Tuff4	1.6	14	1.5	0.30	0.0138	35	9	0.8200	0.8125	2.48	2.73	6.79	7.30
12	Tuff6	0.4	6	0.2	0.09	0.0187	35	9	0.9367	0.0572	1.74	1.28	2.23	2.18
13	Siltstone	8.4	75	4.0	0.95	0.0101	50	10	0.8988	0.0848	1.62	3.47	5.63	5.32
14	Gritstone	4.8	32	1.5	0.42	0.0086	50	10	0.9120	0.0608	1.31	0.53	0.69	0.72
15	Limestone	0.7	10	1.0	0.22	0.0139	50	10	0.8047	1.0476	1.56	0.66	1.03	0.92
16	Mortar	0.3	2	0.2	0.06	0.0091	50	10	0.8197	0.6882	1.00	0.51	0.51	0.45
17	Siltstone	8.4	75	4.0	0.95	0.0101	50	15	0.8988	0.0848	1.22	7.80	9.51	10.46
18	Gritstone	4.8	32	1.5	0.42	0.0086	50	15	0.9120	0.0608	1.34	1.21	1.62	1.70
19	Limestone	0.7	10	1.0	0.22	0.0139	50	15	0.8047	1.0476	1.43	0.53	0.76	0.65
20	Mortar	0.3	2	0.2	0.06	0.0091	50	15	0.8197	0.6882	1.03	0.25	0.26	0.30

Table 6. Rock characteristic parameters in the validation set and calculation results of PCF.

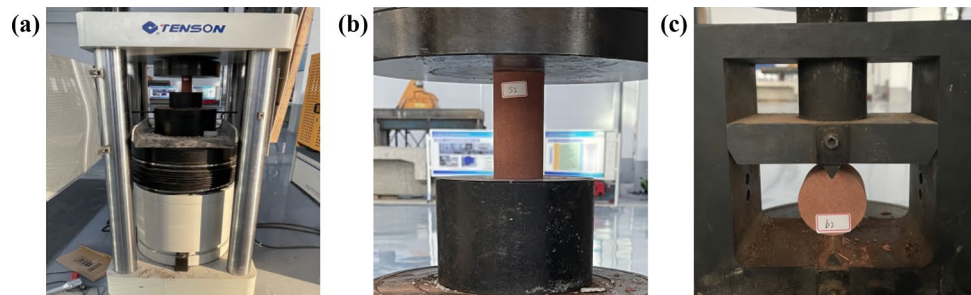


Figure 12. Rock mechanical properties test. (a) the TENSON concrete pressure testing machine, (b) the uniaxial compression test of gritstone, (c) the brazilian splitting test of gritstone.

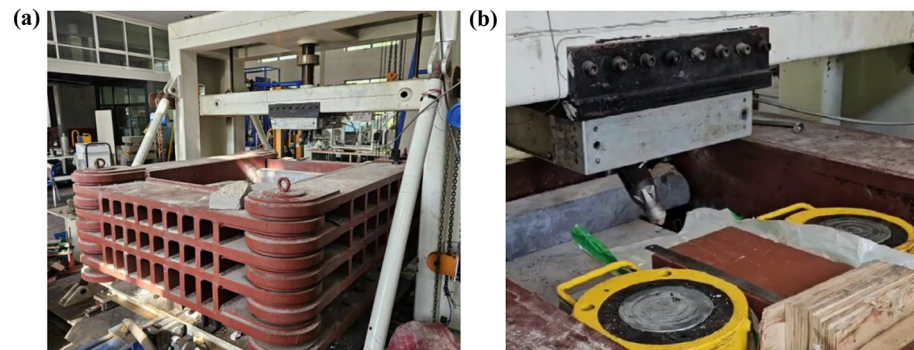


Figure 13. Single-tooth cutting test. (a) the Single-tooth cutting experimental bench, (b) the gritstone cutting test.

PCF Model	This method (uncorrected)	This method (corrected)	Evans	Roxborough	Goktan
R^2	0.81591	0.90404	0.77120	0.77824	0.80346
RMSE	2.20511	1.74707	2.62341	2.45002	2.38121
MAE	1.51056	0.98513	1.51031	1.49211	1.56205

Table 7. Comparative analysis of prediction accuracy in the validation set across different models. Significant values are in bold.

improving the predictive accuracy. This result further validates the reliability of the PCF correction method using the energy correction function with the damage intensity index described in Sect. “[Damage intensity index](#) and [PCF correction](#)”.

Conclusion

This study deeply investigates the existing problems in the prediction theory of PCF of the conical picks. During the interaction between the pick and rock, the PCF is influenced by the uncertain rock bedding structures and internal defects. The existing prediction theories assume specific bedding structures or follow specific rock fragmentation patterns, leading to issues such as low prediction accuracy, high sensitivity to rock properties, and neglecting the effects of pick body and crack propagation on cutting force. To address these issues, this study integrates Griffith theory, rock damage constitutive models, and the damage intensity index to consider the energy aspects of rock fracture and damage evolution. A three-dimensional pick-rock contact model is established, and an innovative calculation method for the conical picks is proposed. The superiority of this model is validated through statistical analysis. The following are the main advantages:

- (1) Development of a 3D pick-rock PCF calculation method: This study employs the projection contour method, Box-Lucas function, and piecewise linear function to accurately determine the profiles of actual pick tip, weld seam, and pick body. By simplifying the stress ellipsoid and incorporating the D. L. Sikarskie stress distribution function and stress triangle transformation, the stress on the pick-rock contact surface is effectively integrated, yielding precise equations for the PCF.
- (2) Incorporating brittleness as a fracture energy criterion for rocks: Conventional fracture theories based on tensile, compressive, and shear strengths are inadequate for the complex and variable properties of rocks due to internal bedding and defects. This study introduces the Griffith fracture theory, which incorporates the compensation of crack surface energy mechanism based on the elastic energy exerted during pick-rock contact from an energy perspective. This effectively addresses the low lithological tolerance of other theoretical approaches. Moreover, the fracture model incorporates rock brittleness as an evaluation criterion by introducing the elastic energy normalization factor K_f , further enhancing the applicability of the Griffith theory.
- (3) Energy correction function fitting and PCF correction: This study combines the energy laws of elastic–plastic energy laws during rock damage evolution with rock brittleness. Using a dataset of 20 rock samples, an energy correction function is established to modify the PCF, utilizing the damage strength index (K_c). Through correlation and t-test analyses of fitted parameters, strong correlation between the brittleness index and the normalized elastic modulus is confirmed. Furthermore, the application of this expression for correcting PCF in a validation set of 20 rock samples demonstrates improved predictive accuracy through error analysis, thus establishing the universality of the PCF correction algorithm.

In summary, this study investigates the energy relationship involved in the process of fracturing and damage evolution in rocks. By employing a 3D pick-rock contact model and incorporating Griffith’s fracture theory and the constitutive theory of rock damage, this paper introduces an energy correction function to determine the damage intensity index (K_c) and correct the PCF. Statistical analysis demonstrates that the uncorrected method proposed in this paper exhibits superior fitting performance compared to other models, with a 20% increase in the coefficient of determination. Moreover, the inclusion of the energy correction function accounting for lithological tolerance further enhances the predictive accuracy of the current method, leading to increased values of R^2 and decreased values of MSE and $RMSE$. The validation through statistical analysis of a validation dataset confirms that the proposed energy correction function is equally effective in optimizing PCF predictions for other rock samples. In conclusion, the PCF and correction algorithm proposed in this study demonstrate optimal predictive accuracy and high lithological tolerance towards variations in rock properties, thus establishing their reliability for applications in other research endeavors.

Data availability

All data generated or analyzed during this study are included in this published article.

Received: 8 February 2024; Accepted: 6 August 2024

Published online: 10 August 2024

References

1. Prokopenko, S., Vorobiev, A. & Andreeva, L. Waste cutters utilization in underground coal mining. *Acta Montan. Slovaca* **23**(1), 81–89 (2018).

2. Gao, K. *et al.* A theoretical model for predicting the Peak Cutting Force of conical picks. *Frat. ed Integrità Strutt.* **27**, 43–52. <https://doi.org/10.3221/IGF-ESIS.27.06> (2014).
3. Zhang, Z. & Gao, F. Research on the nonlinear characteristics of rock energy evolution under uniaxial compression. *Chin. J. Rock Mech. Eng.* **31**(6), 1198–1207 (2012) ((in Chinese)).
4. Miedema, S. A. *The Delft Sand, Clay and Rock Cutting Model. Family Edition.* 3rd edn. (IOS Press, 2015).
5. Evans, I. A theory of the cutting force for point-attack pick. *Int. J. Min. Eng.* **2**, 63–67 (1984).
6. Roxborough FF, Liu ZC (1995) Theoretical considerations on pick shape in rock and coal cutting. Proceedings of the sixth underground operator's conference, Kalgoorlie, WA, Australia, 189–193.
7. Goktan RM (1997) A suggested improvement on Evans cutting theory for conical picks. In: Gurgenci H, Hood M, editors. Proceedings of the fourth international symposium on mine mechanization and automation, Brisbane, Queensland, 1: 57–61.
8. Goktan, R. M. & Gunes, N. A semi-empirical approach to cutting force prediction for point attack picks. *J. S. Afr. Inst. Min. Metall.* **105**, 257–263 (2005).
9. Fathipour-Azar, H. Mean cutting force prediction of conical picks using ensemble learning paradigm. *Rock Mech. Rock Eng.* **56**, 221–236. <https://doi.org/10.1007/s00603-022-03095-0> (2023).
10. Morshedlou, A., Rostami, J. & Moradian, O. Introducing a new model for prediction of mean cutting forces acting on conical pick cutters. *Rock Mech. Rock Eng.* **57**, 1695–1716. <https://doi.org/10.1007/s00603-023-03636-1> (2024).
11. Hekimoglu, O. Z. *Study in the Excavation of Selected Rock Materials with Mechanical Tools* (Newcastle University, 1984).
12. Rånman, K. E. A model describing rock cutting with conical picks. *Rock Mech. Rock Eng.* **18**, 131–140. <https://doi.org/10.1007/bf01019602> (1985).
13. Copur, H. *et al.* A set of indices based on indentation tests for assessment of rock cutting performance and rock properties. *J. S. Afr. Inst. Min. Metall.* **103**(9), 589–599 (2003).
14. Bilgin, N. *et al.* Dominant rock properties affecting the performance of conical picks and the comparison of some experimental and theoretical results. *Int. J. Rock Mech. Min. Sci.* **43**(1), 139–156. <https://doi.org/10.1016/j.ijrmms.2005.04.009> (2006).
15. Tiryaki, B., Boland, J. N. & Li, X. S. Empirical models to predict mean cutting forces on point-attack pick cutters. *Int. J. Rock Mech. Min. Sci.* **47**(5), 858–864. <https://doi.org/10.1016/j.ijrmms.2010.04.012> (2010).
16. Rojek, J. *et al.* Discrete element simulation of rock cutting. *Int. J. Rock Mech. Min. Sci.* **48**(6), 996–1010. <https://doi.org/10.1016/j.ijrmms.2011.06.003> (2011).
17. Dong, L. *et al.* Rock scutting characteristics with single pick and prediction of cutting force based on force chain. *Rock Soil Mech.* **43**(11), 3036–3046. <https://doi.org/10.16285/j.rsm.2022.5008> (2022).
18. Su, O. & Akcin, N. A. Numerical simulation of rock cutting using the discrete element method. *Int. J. Rock Mech. Min. Sci.* **48**(3), 434–442. <https://doi.org/10.1016/j.ijrmms.2010.08.012> (2011).
19. Bao, R. H. *et al.* Estimating the peak indentation force of the edge chipping of rocks using single point-attack pick. *Rock Mech. Rock Eng.* **44**, 339–347. <https://doi.org/10.1007/s00603-010-0133-2> (2011).
20. Kang, H. *et al.* A new linear cutting machine for assessing the rock-cutting performance of a pick cutter. *Int. J. Rock Mech. Min. Sci.* **88**, 129–136. <https://doi.org/10.1016/j.ijrmms.2016.07.021> (2016).
21. Copur, H. *et al.* Effects of different cutting patterns and experimental conditions on the performance of a conical drag tool. *Rock Mech. Rock Eng.* **50**, 1585–1609. <https://doi.org/10.1007/s00603-017-1172-8> (2017).
22. Hekimoglu, Q. Z. A pick force calculation method suggested for tool lacing of mechanical excavators employing drag tools. *Int. J. Min. Reclam. Environ.* **32**(8), 564–585. <https://doi.org/10.1080/17480930.2017.1317946> (2017).
23. Lu, Z., Zeng, Q. & Meng, Z. Numerical research on cutting force and fracture morphology of rock plate with two sides fixed and two sides free. *Math. Probl. Eng.* **2020**, 8652637. <https://doi.org/10.1155/2020/8652637> (2020).
24. Gao, L. *et al.* An energy preservation index for evaluating the rockburst potential based on energy evolution. *Energies* **13**(14), 1–16. <https://doi.org/10.3390/en13143636> (2020).
25. Zhang, Z. & Gao, F. Experimental investigation on the energy evolution of dry and water-saturated red sandstones. *Int. J. Min. Sci. Technol.* **25**(3), 383–388. <https://doi.org/10.1016/j.ijmst.2015.03.009> (2015).
26. Niu, S. J. *et al.* Mechanical properties and energy mechanism of saturated sandstones. *J. Central South Univ.* **25**(6), 1447–1463. <https://doi.org/10.1007/s11771-018-3839-z> (2018).
27. Zhang, Z. & Gao, F. Experimental study on the energy evolution characteristics of coal, sandstone and granite during loading process. *J. China Univ. Min. Technol.* **44**(3), 416–422. <https://doi.org/10.13247/j.cnki.jcmt.000321> (2015).
28. Hou, P. *et al.* Effect of the layer orientation on mechanics and energy evolution characteristics of shales under uniaxial loading. *Int. J. Min. Sci. Technol.* **26**(5), 857–862. <https://doi.org/10.1016/j.ijmst.2016.05.041> (2016).
29. Zhang, L. *et al.* Energy evolution analysis and failure criteria for rock under different stress paths. *Acta Geotech.* **16**, 569–580. <https://doi.org/10.1007/s11440-020-01028-1> (2021).
30. Duan, M. *et al.* Peak cutting force estimation of improved projection profile method for rock fracturing capacity prediction with high lithological tolerance. *Coatings* **12**(9), 1306. <https://doi.org/10.3390/coatings12091306> (2022).
31. Saadat, M., Taheri, A. & Kawamura, Y. Incorporating asperity strength into rock joint constitutive model for approximating asperity damage: An insight from DEM modelling. *Eng. Fract. Mech.* <https://doi.org/10.1016/j.engfracmech.2021.107744> (2021).
32. Sikarskie, D. L. & Altiero, N. J. The formation of chips in the penetration of elastic-brittle materials (Rock). *J. Appl. Mech.* **40**(3), 791–798. <https://doi.org/10.1115/1.3423091> (1973).
33. Lyu, C. *et al.* Study on very long-term creep tests and nonlinear creep-damage constitutive model of salt rock. *Int. J. Rock Mech. Min. Sci.* **146**, 104873. <https://doi.org/10.1016/j.ijrmms.2021.104873> (2021).
34. Liu, X. S. *et al.* Damage constitutive model based on energy dissipation for intact rock subjected to cyclic loading. *Int. J. Rock Mech. Min. Sci.* **85**, 27–32. <https://doi.org/10.1016/j.ijrmms.2016.03.003> (2016).
35. Xiao, P. *et al.* Stability analysis of surrounding rock mass in underground powerhouse considering damage effect of microfractures. *J. Rock Mech. Geotech. Eng.* **14**, 1115–1130. <https://doi.org/10.1016/j.jrmge.2022.01.007> (2022).
36. Gu, Q. *et al.* Damage constitutive model of brittle rock considering the compaction of crack. *Geomech. Eng.* **15**(5), 1081–1089. <https://doi.org/10.12989/gae.2018.15.5.1081> (2018).
37. Xie, H. *et al.* Energy mechanism of deformation and failure of rock masses. *Chin. J. Rock Mech. Eng.* **27**(9), 1729–1740 (2008).
38. Wang, G., Wen, X. & Zhang, L. Dip effect of energy evolution mechanism in jointed sandstone under uniaxial compression. *J. Central South Univ. (Sci. Technol.)* **51**(7), 1913–1923. <https://doi.org/10.11817/j.issn.1672-7207.2020.07.017> (2020).

Acknowledgements

This work financially supported by Hainan University research start-up fund (Grant no. KYQD(ZR)23085). The authors gratefully acknowledge the supports.

Author contributions

M.D., L. S. and Z. Z. wrote the manuscript, while Y.H., Q. H. and J. L. reviewed the manuscript and made many important comments.

Funding

Hainan University research start-up fund, KYQD(ZR)23085.

Competing interests

The authors declare no competing interests.

Additional information

Correspondence and requests for materials should be addressed to Z.Z.

Reprints and permissions information is available at www.nature.com/reprints.

Publisher's note Springer Nature remains neutral with regard to jurisdictional claims in published maps and institutional affiliations.

Open Access This article is licensed under a Creative Commons Attribution-NonCommercial-NoDerivatives 4.0 International License, which permits any non-commercial use, sharing, distribution and reproduction in any medium or format, as long as you give appropriate credit to the original author(s) and the source, provide a link to the Creative Commons licence, and indicate if you modified the licensed material. You do not have permission under this licence to share adapted material derived from this article or parts of it. The images or other third party material in this article are included in the article's Creative Commons licence, unless indicated otherwise in a credit line to the material. If material is not included in the article's Creative Commons licence and your intended use is not permitted by statutory regulation or exceeds the permitted use, you will need to obtain permission directly from the copyright holder. To view a copy of this licence, visit <http://creativecommons.org/licenses/by-nc-nd/4.0/>.

© The Author(s) 2024